Non-monotonicity of the frictional bimaterial effect

Michael Aldam[1], Shiqing Xu[2], Efim A. Brener[3], Yehuda Ben-Zion[4] and Eran Bouchbinder[1]

[1] *Chemical Physics Department, Weizmann Institute of Science, Rehovot 7610001, Israel*
[2] *National Research Institute for Earth Science and Disaster Resilience, Tsukuba, Ibaraki 305-0006, Japan*
[3] *Peter Grünberg Institut, Forschungszentrum Jülich, D-52425 Jülich, Germany*
[4] *Department of Earth Sciences, University of Southern California, Los Angeles, CA 90089, USA*

Sliding along frictional interfaces separating dissimilar elastic materials is qualitatively different from sliding along interfaces separating identical materials due to the existence of an elastodynamic coupling between interfacial slip and normal stress perturbations in the former case. This bimaterial coupling has important implications for the dynamics of frictional interfaces, including their stability and rupture propagation along them. We show that while this bimaterial coupling is a monotonically increasing function of the bimaterial contrast, when it is coupled to interfacial shear stress perturbations through a friction law, various physical quantities exhibit a *non-monotonic* dependence on the bimaterial contrast. In particular, we show that for a regularized Coulomb friction, the maximal growth rate of unstable interfacial perturbations of homogeneous sliding is a non-monotonic function of the bimaterial contrast, and provide analytic insight into the origin of this non-monotonicity. We further show that for velocity-strengthening rate-and-state friction, the maximal growth rate of unstable interfacial perturbations of homogeneous sliding is also a non-monotonic function of the bimaterial contrast. Results from simulations of dynamic rupture along a bimaterial interface with slip-weakening friction provide evidence that the theoretically predicted non-monotonicity persists in non-steady, transient frictional dynamics.

I. INTRODUCTION

Bimaterial configurations with two solids of different elastic properties in contact exist widely in earth and man-made systems. One class of examples involves large strike-slip faults that separate different crustal blocks, as reported for the San Andreas, Hayward and San Jacinto faults in California [5, 16, 33, 72] and the North Anatolian fault in Turkey [52, 66]. Historic records and recent observations indicate that such strike-slip faults are able to produce earthquakes with magnitude up to 8 [21, 62, 70]. The contrast of seismic properties across large faults may become more prominent with increasing fault displacement. In addition, large faults tend to nucleate along prominent pre-existing sutures as reported for the North Anatolian fault [68]. In a different tectonic regime, subduction zone plate interfaces juxtapose continental crust against denser oceanic crust [76] and host megathrust earthquakes with magnitude that may be above 9 [40]. The appearance in subduction setting of compliant sediments in the overriding plate near the toe can contribute significantly to causing large slip near the trench and anomalous tsunami excitation during large earthquakes [46, 67, 71]. Bimaterial fault configurations may also develop spontaneously from initially homogeneous solids by damage mechanisms that create a low velocity layer [47, 75, 85, 86]. Once such layer is formed, future slip events or deformation bands tend to migrate to the boundary between the low velocity zone and relatively intact host rocks [24, 38]. Another important class of bimaterial configurations is ice-rock interfaces as in the Whillans Ice Plain region of the Western Antarctica [45, 53, 81]. Bimaterial interfaces exist also at the bottom of landslides and may be relevant for the continuing propagation of long-runout landslides in ar-

eas with little to no topographic gradient [23, 41]. Other examples include interfaces in mines (edges of mined layers) and a variety of composite engineering materials and structures.

The presence of material contrast across a fault produces a generic failure instability mechanism associated with elastodynamic coupling between interfacial slip and changes in normal stress [80], along with head waves that propagate along the interface and contribute to dynamic changes of stress [11, 12]. These effects and several geophysical paradoxes (e.g. the heat flow paradox and the absence of rupture branching from large faults) that arise in theoretical considerations in a homogeneous solid motivated numerical simulations of bimaterial ruptures that explore parameters producing self-sustained ruptures even without frictional weakening [8, 14]. Such simulations with a constant friction coefficient (and no other intrinsic physical length scale) do not have a continuum limit, so the numerical solutions are ill-posed [58]. Consequently, the results contain a mixture of physical features and numerical artifacts, but careful examination of sets of solutions with different physical and numerical parameters may still allow extracting tentative conclusions on the system behavior [13]. The results from the early numerical studies suggested that bimaterial ruptures can produce narrow self-healing slip pulses with low dynamic stress (and low associated frictional heat) that may resolve key outstanding paradoxes [14]. These and later studies highlighted several additional features of bimaterial ruptures that can have significant effects on fault mechanics and on generated ground motion, including preferred rupture directivity, generation of rock damage asymmetry across faults and tensional source term with potential for fault opening and rock pulverization [6, 17, 26, 83]. Many additional studies at-

tempted to clarify properties of bimaterial ruptures in the presence of various nucleation procedures and friction laws [6, 15, 34, 37, 64, 73] and off-fault material yielding in relation to the background principal stress orientation [28, 84].

The interesting dynamical features of bimaterial ruptures led to various observational studies involving laboratory experiments and in-situ data. The former focused on measuring rupture velocity and directivity along with dynamic changes in normal stress in various settings [20, 48, 74, 82]. The latter focused on estimating rupture directivity (e.g. [25, 42, 63, 78]) and rock damage asymmetry (e.g. [29, 30, 43, 50]) in relation to contrast of seismic velocities across faults. The observational results generally support the relevance of bimaterial ruptures to various aspects of fault mechanics and seismic hazard. It is therefore important to quantify how dynamic bimaterial effects change with the degree of property contrast across the interface. *Ben-Zion and Andrews* [14] found that under a constant Coulomb friction the growth rate of the maximal slip velocity in a slip pulse is a non-monotonic function of material contrast across the interface and is maximal around the level where generalized Rayleigh waves barely exist. As mentioned, however, numerical simulations with constant Coulomb friction do not have a continuum limit, so they cannot be used to derive general conclusions.

In the present work we study the dependence of dynamic bimaterial effects on the degree of bimaterial contrast using a variety of theoretical and numerical analyses. This is done by examining the stability of steady state sliding and of unsteady rupture propagation in the context of frictional laws that have well-posed continuum descriptions. Our major result is that while the bimaterial coupling between interfacial slip and normal stress changes is a monotonically increasing function of the bimaterial contrast, when it is coupled to interfacial shear stress perturbations through a friction law, various physical quantities exhibit a non-monotonic dependence on the bimaterial contrast. We also show that this non-monotonicity is not directly related to the existence/inexistence of generalized Rayleigh waves. The generic non-monotonicity of the bimaterial effect is established in a few steps. First, section II establishes the monotonicity of the bimaterial coupling between interfacial slip and normal stress perturbations. Section III outlines the basic theoretical framework that connects slip with shear and normal stress changes along a bi-

material interface once a friction law is taken into account. Sections IV-V introduce different types of friction laws — a regularized Coulomb friction and a velocity-strengthening rate-and-state friction — and show analytically and semi-analytically that the maximal growth rate of unstable linear perturbations of steady sliding exhibits a non-monotonic dependence on the degree of bimaterial contrast. Finally, section VI demonstrates the existence of non-monotonic behavior in numerical simulations of transient rupture evolution under a linear slip-weakening friction law. The results and their implications are summarizes and discussed in the concluding section VII.

II. MONOTONICITY OF THE BIMATERIAL COUPLING BETWEEN INTERFACIAL SLIP AND NORMAL STRESS PERTURBATIONS

We start by considering two linear elastic half-spaces in mechanical contact at an interface located at $y = 0$. The coordinate along the interface is x and plane-strain conditions are assumed. The bimaterial coupling between interfacial slip and normal stress emerges in this physical situation from the elastodynamics of the two half-spaces when they are made of different linear elastic materials, i.e. at least one of their linear elastic moduli or mass density is different. To see how this coupling emerges, note that each half-space satisfies the Navier-Lamé equation $\nabla \cdot \boldsymbol{\sigma} = \frac{\mu}{1-2\nu}\nabla(\nabla \cdot \boldsymbol{u}) + \mu\nabla^2\boldsymbol{u} = \rho\,\ddot{\boldsymbol{u}}$, with its own shear modulus μ, Poisson's ratio ν, mass density ρ, displacement vector field $\boldsymbol{u}$ and Cauchy stress tensor field $\boldsymbol{\sigma}$ [39]. Hooke's law was used to relate $\boldsymbol{\sigma}$ to $\boldsymbol{u}$, and each superimposed dot represents a partial time derivative. As the bimaterial coupling between interfacial slip and normal stress manifests itself in the presence of spatiotemporally varying fields, we express the deviations from homogeneous fields at the interface, approached from its upper and lower sides $y = 0^{\pm}$, by $\boldsymbol{\sigma}(x,t) = \delta\boldsymbol{\sigma}\,\exp[-ik\,(zc_st + x)]$ and $\boldsymbol{u}(x,t) = \delta\boldsymbol{u}\exp[-ik\,(zc_st + x)]$, where k is the wavenumber along the interface, $-z$ is the complex dimensionless phase-velocity and $c_s = \sqrt{\mu/\rho}$ is the shear wave-speed in each half-space. That is, $\delta\boldsymbol{\sigma}$ and $\delta\boldsymbol{u}$ are the Fourier amplitude of the fields.

Each of the two problems formulated above, for the upper and lower half-spaces, admits a solution that at the interface takes the form $\delta u_i = M_{ij}(z,k)\,\delta\sigma_{yj}$. For the upper half-space — denoted hereafter by the superscript (1) — the matrix $\boldsymbol{M}$ takes the form [58]

$$\boldsymbol{M}^{(1)}(z,k) = \frac{1}{|k|\,\mu\,R(z,\beta)}\begin{pmatrix} \alpha_s\left(\alpha_s^2 - 1\right) & i\,\mathrm{sgn}(k)\left(\alpha_s^2 - 2\alpha_d\alpha_s + 1\right) \\ -i\,\mathrm{sgn}(k)\left(\alpha_s^2 - 2\alpha_d\alpha_s + 1\right) & \alpha_d\left(\alpha_s^2 - 1\right) \end{pmatrix}. \tag{1}$$

Here $\alpha_s(z) \equiv \sqrt{1 - z^2}$ and $\alpha_d(z,\beta) \equiv \sqrt{1 - \beta^2 z^2}$, where $\beta \equiv \frac{c_s}{c_d} = \sqrt{\frac{1-2\nu}{2-2\nu}}$ is the ratio of the shear wave-speed c_s to

the dilatational wave-speed c_d and $R(z, \beta) \equiv 4\alpha_d\alpha_s - (\alpha_s^2 + 1)^2$ is the Rayleigh function [1]. For the lower half-space — denoted hereafter by the superscript (2) — $\boldsymbol{M}^{(2)}(z, k)$ is the same as $\boldsymbol{M}^{(1)}(z, k)$ except that its diagonal elements have opposite signs. Up until now, the elastodynamic solutions in the two half-spaces were considered separately. The coupling between the two solutions appears when continuity and jump conditions across the interface at $y = 0$ are introduced [36]. Specifically, we demand continuity of the normal component of the interfacial displacement vector field (i.e. we assume no opening gaps), $\delta u_y^{(1)} - \delta u_y^{(2)} = 0$, and of σ_{yx} and σ_{yy}, but allow for a discontinuity in the tangential component of the interfacial displacement vector field (interfacial slip), $\delta u_x^{(1)} - \delta u_x^{(2)} \equiv \delta\epsilon$, which later on will appear in the interfacial constitutive relation. Using these interfacial conditions, one obtains [36]

$$\delta\boldsymbol{u}^{(1)} - \delta\boldsymbol{u}^{(2)} = \begin{pmatrix} \delta\epsilon \\ 0 \end{pmatrix} = (\boldsymbol{M}^{(1)} - \boldsymbol{M}^{(2)}) \begin{pmatrix} \delta\sigma_{yx} \\ \delta\sigma_{yy} \end{pmatrix} . \quad (2)$$

By inverting this relation and defining $\boldsymbol{G} \equiv (\boldsymbol{M}^{(1)} - \boldsymbol{M}^{(2)})^{-1}$, we obtain $\delta\sigma_{yx} = G_{11}\,\delta\epsilon$ and $\delta\sigma_{yy} = G_{21}\,\delta\epsilon$. If the two half-spaces are made of *identical* materials, then $\boldsymbol{G}$ is diagonal, implying that $\delta\sigma_{yy} = 0$ independently of the interfacial slip $\delta\epsilon$. Consequently, the elastodynamic bimaterial coupling between interfacial slip perturbations $\delta\epsilon$ and normal stress perturbations $\delta\sigma_{yy}$ is entirely encapsulated in the off-diagonal element G_{21}, which is non-zero only in the presence of bimaterial contrast.

To highlight the dependence of G_{11} and G_{21} on physical variables and material parameters, one needs to make a normalization choice; we choose to normalize stresses by the shear modulus of the upper half-space, $\mu^{(1)}$, and to define the complex phase-velocity $-z$ of the coupled problem with respect to the shear wave-speed of the upper half-space, $c_s^{(1)}$ (note that this normalization has already been used in both $\boldsymbol{M}^{(1)}$ and $\boldsymbol{M}^{(2)}$ in Eq. (2)). With these definitions, we obtain

$$\delta\sigma_{yx} = \mu^{(1)}\,k\,G_1(z; \psi, \chi, \nu^{(1)}, \nu^{(2)})\,\delta\epsilon \quad \text{and}$$
$$\delta\sigma_{yy} = -i\mu^{(1)}\,k\,G_2(z; \psi, \chi, \nu^{(1)}, \nu^{(2)})\,\delta\epsilon , \quad (3)$$

where $G_1 \equiv G_{11}/k\mu^{(1)}$, $G_2 \equiv iG_{21}/k\mu^{(1)}$, $\psi \equiv \mu^{(2)}/\mu^{(1)}$ and $\chi \equiv \rho^{(1)}/\rho^{(2)}$. The explicit forms of G_1 and G_2 are presented in the Appendix. Note that ψ and χ are defined such that the shear wave-speeds ratio $\zeta \equiv c_s^{(2)}/c_s^{(1)} = \sqrt{\psi\chi}$ is an increasing function of both. We thus observe that the elastodynamic transfer functions G_1 and G_2, which fully characterize the elastodynamic part of the bimaterial problem, depend on the complex phase-velocity $-z$ (but not on the magnitude of the wavenumber k) and on 4 dimensionless material parameters: the shear moduli ratio ψ, the mass densities ratio χ, and the two Poisson's ratios $\nu^{(1)}$ and $\nu^{(2)}$. G_1 and G_2 are real and symmetric functions of z. The first question we would like to address is the dependence of G_2, which quantifies the elastodynamic bimaterial coupling between interfacial slip perturbations $\delta\epsilon$ and normal stress perturbations $\delta\sigma_{yy}$, on

the material contrast as quantified by ψ and χ. To that aim, we plot in Fig. 1 G_2 as a function of ψ (top left, with $\chi = 1$) and χ (top right, with $\psi = 1$), for various values of z (in a range whose relevance will become clearer below) and $\nu^{(1)} = \nu^{(2)} = 0.25$. The major observation is that G_2 is a monotonically increasing function of ψ and χ. The same behavior persists for other values of the fixed parameters and for varying $\nu^{(1)}$ when $\nu^{(2)}$ is fixed, with $\psi = \chi = 1$ (not shown). In fact, G_2 is also an increasing function of z, as is clearly observed in Fig. 1. Note that, as expected, in the absence of bimaterial contrast ($\psi \to 1$, $\chi \to 1$ and $\nu^{(1)} \to \nu^{(2)}$), G_2 vanishes. We also present G_1 (lower panels, for the same choices of parameters), which exhibits a monotonically increasing dependence on ψ and χ as well. Note that G_1 remains finite also in the absence of bimaterial contrast and that it is a decreasing function of z.

III. COUPLING INTERFACIAL NORMAL AND SHEAR STRESS PERTURBATIONS THROUGH A FRICTION LAW

In the previous section it was demonstrated that the elastodynamic transfer functions G_1 and G_2 exhibit a monotonic dependence on the bimaterial contrast quantified by ψ and χ. Can we conclude then that various physical observables, especially those which identically vanish in the absence of a bimaterial contrast, generically exhibit a monotonically increasing dependence on the bimaterial contrast? We would like to argue that the answer to this question is non-trivial; that is, that the monotonic dependence of G_1 and G_2 on the bimaterial contrast parameters ψ and χ does *not* immediately imply a monotonic dependence of any physical observable of interest on ψ and χ. The key point is that Eq. (3) is *not* a complete solution of the physical problem at hand because $\delta\sigma_{yx}$ and $\delta\sigma_{yy}$ are *not* independent; rather, they are generically coupled by an interfacial constitutive relation, i.e. by a friction law. Moreover, the relation between the wavenumber k and the complex dimensionless phase-velocity $-z$ remains unspecified in Eq. (3). That is, the relations in Eq. (3) emerge from the bulk elastodynamics of the two half-spaces and the continuity of the normal component of the interfacial displacement vector, but still leave the relation between $\delta\sigma_{yx}$, $\delta\sigma_{yy}$ and $\delta\epsilon$ unconstrained. The relation between these quantities depends on the physics of the interface and is expressed in terms of an interfacial constitutive relation.

Quite generically, the interfacial constitutive relation — the friction law — can be written in the form

$$\dot{\tau} = F(\tau, \sigma, v, \epsilon, ...) , \quad (4)$$

where we defined $\tau(x, t) \equiv \sigma_{yx}(x, y = 0, t)$, $\sigma(x, t) \equiv -\sigma_{yy}(x, y = 0, t)$, $\epsilon(x, t) \equiv u_x^{(1)}(x, y = 0, t) - u_x^{(2)}(x, y = 0, t)$ and $v(x, t) \equiv \dot{u}_x^{(1)}(x, y = 0, t) - \dot{u}_x^{(2)}(x, y = 0, t) = \dot{\epsilon}(x, t)$. The dots in the arguments of the function F in Eq. (4)
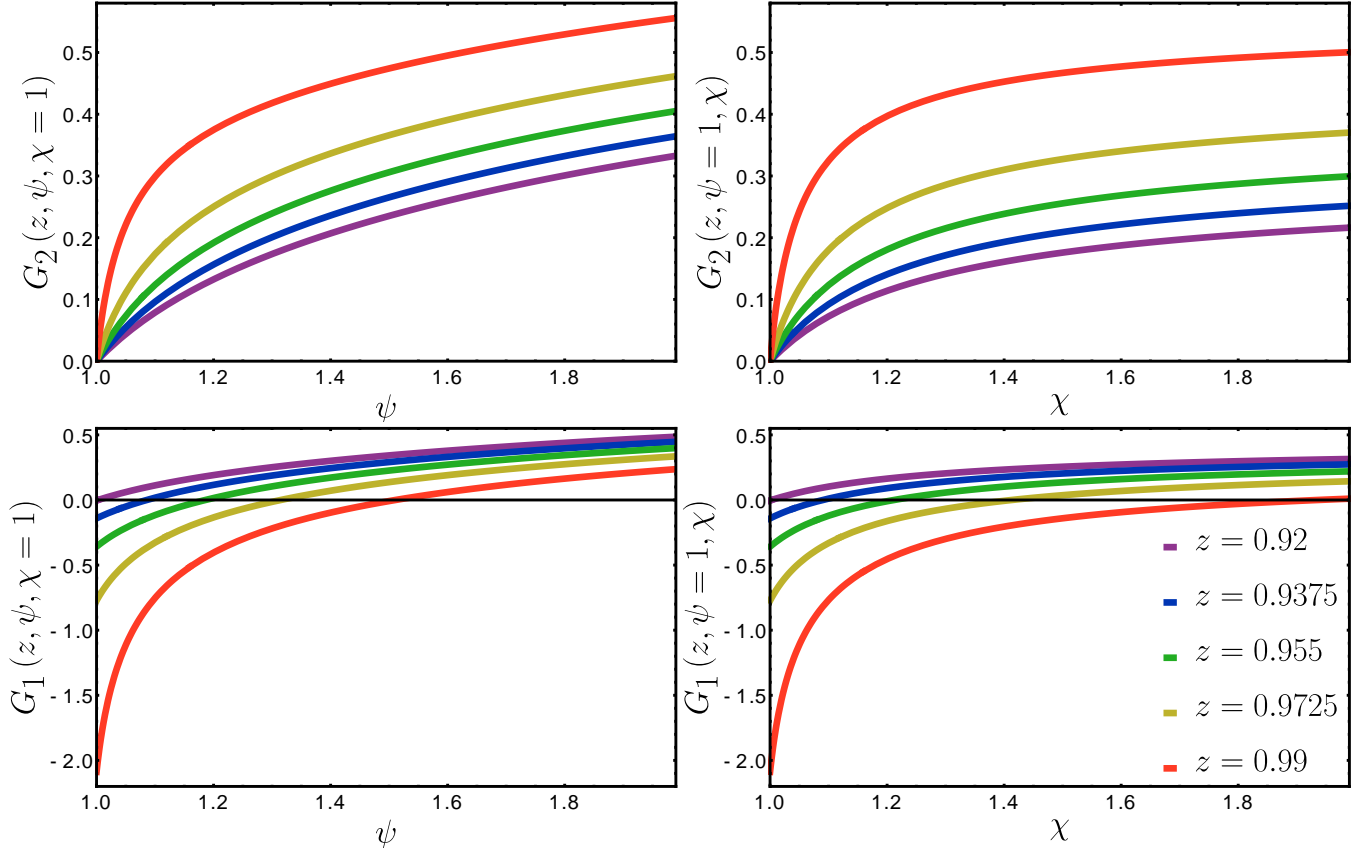
FIG. 1. (Top panels) G_2 as a function of ψ for $\chi = 1$ (left) and χ for $\psi = 1$ (right) for a few values of z (see legend in the bottom right panel). (Bottom panels) G_1 as a function of ψ (left) and χ (right) for the same values of z. In all panels $\nu^{(1)} = \nu^{(2)} = 0.25$.

represent possible additional fields — the so-called internal state fields — which describe the structural state of the interface and satisfy their own evolution equations. Equation (4) gives rise to coupling between the Fourier amplitudes $\delta\sigma_{yx}$, $\delta\sigma_{yy}$ and $\delta\epsilon$ appearing in Eq. (3), thus fully define the physical problem at hand. The question then is whether physical quantities in this fully defined problem generically exhibit monotonic dependence on the bimaterial contrast or not. This question will be extensively addressed in what follows.

IV. NON-MONOTONICITY OF THE BIMATERIAL EFFECT IN THE STABILITY OF HOMOGENEOUS SLIDING WITH A REGULARIZED COULOMB FRICTION

To start addressing the posed question, we first consider the following interfacial constitutive relation [55–57]

$$\dot\tau = -\frac{v}{L}\left(\tau - f\sigma\right) , \qquad (5)$$

which is a specific example of Eq. (4). Here $f > 0$ is a constant friction coefficient and L is a lengthscale that controls the relaxation time L/v to Coulomb friction $\tau = f\sigma$. In the limit $L \to 0$, Eq. (4) is reduced to Coulomb

friction $\tau = f\sigma$ [31, 54], which is known to be ill-posed (see below and [58]). The finite L regularization renders the interfacial constitutive relation in Eq. (5) well-posed (see below) and hence suitable for our purposes here.

To see how the interfacial constitutive relation in Eq. (5) couples $\delta\sigma_{yx}$, $\delta\sigma_{yy}$ and $\delta\epsilon$, we consider homogeneous sliding at a velocity V under the application of a compressive stress σ_0, such that $\tau_0 = f\sigma_0$. We then consider a slip displacement perturbation of amplitude ξ on top of the homogeneous sliding solution, i.e. $\epsilon(x,t) = Vt + \xi \exp\left[-ik\left(tzc_s^{(1)} + x\right)\right]$, and use Eq. (3) to obtain

$$\sigma_{yx}(x,t) = f\sigma_0 + \xi\,k\,\mu\,G_1(z)\,\exp\left[-ik\left(tzc_s^{(1)} + x\right)\right] ,$$
$$\sigma_{yy}(x,t) = -\sigma_0 - i\,\xi\,k\,\mu\,G_2(z)\,\exp\left[-ik\left(tzc_s^{(1)} + x\right)\right] ,$$
$$\qquad (6)$$

where the parametric dependence of $G_{1,2}(z)$ on ψ, χ, $\nu^{(1)}$ and $\nu^{(2)}$ is omitted for the ease of notation. Inserting these fields into Eq. (5), we obtain to leading order in ξ

$$(1 - izq)\,G_1(z) - if\,G_2(z) = 0 , \qquad (7)$$

where we defined the dimensionless wavenumber as $q \equiv kLc_s^{(1)}/V$. The solutions to Eq. (7) determine the linear stability of homogeneous sliding along frictional interfaces described by the regularized Coulomb friction of

Eq. (5). In particular, solutions with $\Im[z] > 0$ are unstable, i.e. they correspond to perturbations that exponentially grow in time, while solutions with $\Im[z] < 0$ are stable, i.e. they correspond to perturbations that exponentially decay in time.

When dealing with instabilities, one is generally interested in identifying the competing, i.e. stabilizing and destabilizing, physical processes involved in a given problem. In our case, the relevant physics includes the regularized Coulomb friction law and the bimaterial effect. The former, which does not feature any frictional weakening behavior, is not expected to give rise to destabilization. The latter, which may give rise to a reduction in the interfacial normal stress and hence to weakening, appears to be responsible for the only potentially destabilizing process in the problem. As the bimaterial coupling between interfacial slip and normal stress variations is fully described by the elastodynamic transfer function $G_2(z)$, our strategy is to consider first the frictionless limit $f \to 0$, for which the combination fG_2 in Eq. (7) vanishes, and then take into account the potentially destabilizing bimaterial effect perturbatively.

For $f \to 0$, Eq. (7) admits non-trivial solutions $z = \pm z_{\mathrm{GR}}$, with a real z_{GR}, corresponding to $G_1(z = \pm z_{\mathrm{GR}}) = 0$. These propagative wave solutions, known as Generalized Rayleigh waves (hence the subscript), exist for a finite range of bimaterial contrasts [2, 79]. For example, for $\chi = 1$, they exist in the range $0 < \psi < 1.85$ (for $\nu^{(1)} = \nu^{(2)} = 0.25$) and for $\psi = 1$, they exist in the range $0 < \chi < 9.51$ (also for $\nu^{(1)} = \nu^{(2)} = 0.25$). Obviously, $z = \pm z_{\mathrm{GR}}$ is *not* a solution of Eq. (7); however, when Generalized Rayleigh waves exist, we can look for solutions in the form $z = \pm z_{\mathrm{GR}} + f\delta z$, where the complex contribution $f\delta z$ is treated as small [58]. Inserting this ansatz into Eq. (7) and expanding to leading order in f, we obtain unstable solutions ($\Im[z] > 0$) in the form

$$z \simeq -z_{\mathrm{GR}} + \frac{ifG_2(z_{\mathrm{GR}})}{(1 + iqz_{\mathrm{GR}})\,|G_1'(z_{\mathrm{GR}})|} \quad \Longrightarrow$$

$$\lambda \equiv q\,\Im[z] \simeq \frac{qfG_2(z_{\mathrm{GR}})}{(1 + q^2 z_{\mathrm{GR}}^2)\,|G_1'(z_{\mathrm{GR}})|} \,, \qquad (8)$$

where $\lambda(q)$ is the dimensionless instability growth rate.

The analytic approximation in Eq. (8) is compared to the full numerical solution of Eq. (7) for two sets of parameters in Fig. 2, demonstrating favorable agreement. Note that $\lambda(q)$ features a maximum, λ_{max}, attained at $q = q_{max}$, which corresponds to the most unstable mode. In addition, $\lambda \to 0$ in the limit $q \to \infty$ (vanishingly small perturbation wavelength), which shows that indeed the problem is well-posed in the presence of a finite L (ill-posedness typically corresponds to the situation in which $\lambda \propto |q|$ in the limit $q \to \infty$, as is the case with Coulomb friction). As $z_{\mathrm{GR}}(\psi, \chi, \nu^{(1)}, \nu^{(2)})$ is a central quantity involved in the analytic approximation in Eq. (8), we plot $z_{\mathrm{GR}}(\psi, \chi = 1, \nu^{(1)} = \nu^{(2)} = 0.25)$ in the inset Fig. 2 (left) and $z_{\mathrm{GR}}(\psi = 1, \chi, \nu^{(1)} = \nu^{(2)} = 0.25)$ in the inset Fig. 2 (right). z_{GR} exhibits a relatively weak dependence on the bimaterial contrast (quantified by either χ or ψ), with

values close to unity, though for the same range of z values, the functions $G_{1,2}$ in Fig. 1 exhibit non-negligible variations.

The approximated analytic solution in Eq. (8) allows us to gain analytic insight into the main question posed above, i.e. whether physical quantities in the considered problem depend monotonically on the bimaterial contrast. The quantity we choose to focus on is the maximal growth rate λ_{max} — a central physical quantity in any linear stability analysis — which is expected to vanish in the absence of bimaterial contrast (as there is no destabilizing process in the problem in this limit). Using Eq. (8), we immediately obtain the following estimates for the most unstable mode and the maximal instability growth rate

$$q_{max} \simeq \frac{1}{z_{\mathrm{GR}}} \,, \qquad \lambda_{max} \simeq \frac{fG_2(z_{\mathrm{GR}})}{2\,z_{\mathrm{GR}}\,|G_1'(z_{\mathrm{GR}})|} \,, \quad (9)$$

which are valid in the range of bimaterial contrasts for which z_{GR} exists (note, though, that while the existence of z_{GR} is important for the analytic approximation, it does not play a crucial role in the main effect of interest here). The prediction in Eq. (9) shows that indeed λ_{max} is proportional to G_2 and hence that it vanishes in the absence of a bimaterial contrast, $G_2 = 0$, as expected. The dependence of λ_{max} on the bimaterial contrast, however, is *not exclusively* determined by G_2, but rather by the ratio of $G_2(z_{\mathrm{GR}})$ and $z_{\mathrm{GR}}|G_1'(z_{\mathrm{GR}})|$, where G_1 and G_2 depend on the bimaterial contrast (quantified by ψ, χ, $\nu^{(1)}$, $\nu^{(2)}$) both explicitly and implicitly through $z_{\mathrm{GR}}(\psi, \chi, \nu^{(1)}, \nu^{(2)})$. The functions G_2, G_1 and z_{GR} exhibit a non-trivial dependence on the bimaterial contrast, as shown in Figs. 1 and 2, and consequently $\lambda_{max}(\psi, \chi, \nu^{(1)}, \nu^{(2)})$ might be non-monotonic despite the fact that G_2 is monotonic. Indeed, plotting $\lambda_{max}(\psi, \chi = 1, \nu^{(1)} = \nu^{(2)} = 0.25)$ in Fig. 3 (left) and $\lambda_{max}(\psi = 1, \chi, \nu^{(1)} = \nu^{(2)} = 0.25)$ in Fig. 3 (right), we observe that both quantities exhibit a non-monotonic dependence on the bimaterial contrast. This result explicitly demonstrates that important physical quantities may exhibit a non-monotonic dependence on the bimaterial contrast, i.e. that there exist some non-trivial contrast conditions in which the frictional bimaterial effect manifests itself most strongly. Note also that the location of the maximal bimaterial effect does not coincide with the disappearance of Generalized Rayleigh waves.

V. NON-MONOTONICITY OF THE BIMATERIAL EFFECT IN THE STABILITY OF HOMOGENEOUS SLIDING WITH VELOCITY-STRENGTHENING RATE-AND-STATE FRICTION

In the previous section we demonstrated that despite the fact that the elastodynamic bimaterial coupling between interfacial slip and normal stress perturbations is a monotonically increasing function of the bimate-
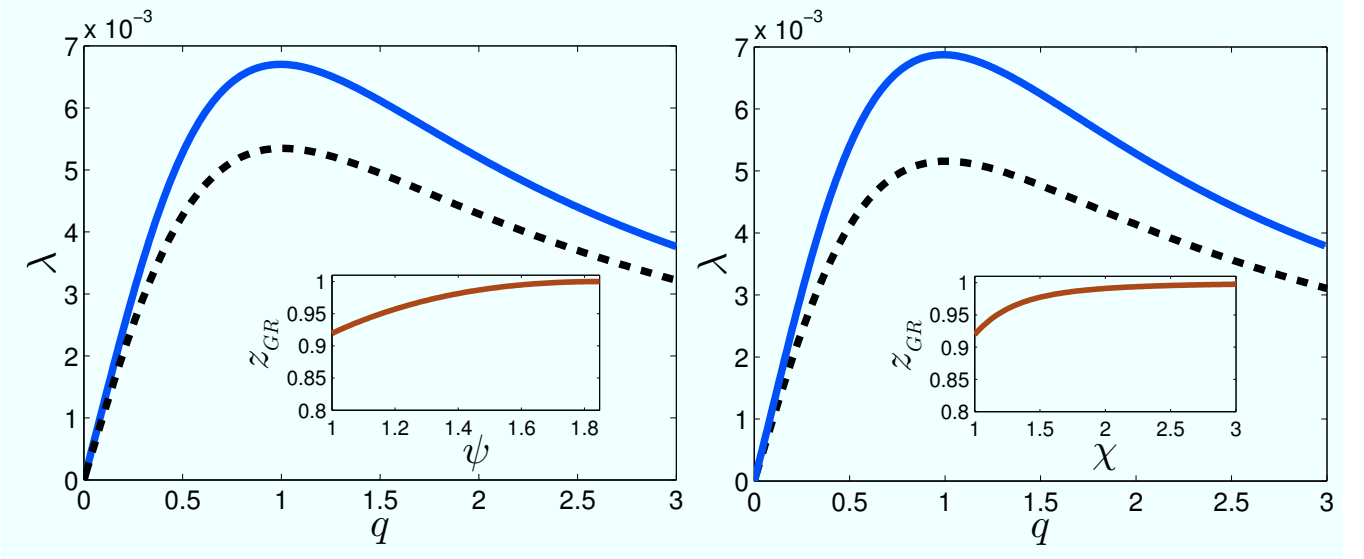
FIG. 2. The instability growth rate λ as a function of the dimensionless wavenumber q (solid lines) obtained from a numerical solution of Eq. (7) with $\psi=1.6$ and $\chi=1$ (left), and with $\psi=1$ and $\chi=2.5$ (right). The dashed lines correspond to the analytic approximation in Eq. (8). As the latter involves the dimensionless phase-velocity of Generalized Rayleigh waves, z_{GR}, we show in the insets the dependence of z_{GR} on ψ for $\chi=1$ (left) and on χ for $\psi=1$ (right). We used $\nu^{(1)}=\nu^{(2)}=0.25$ and $f=0.3$ to obtain the results shown in this figure.
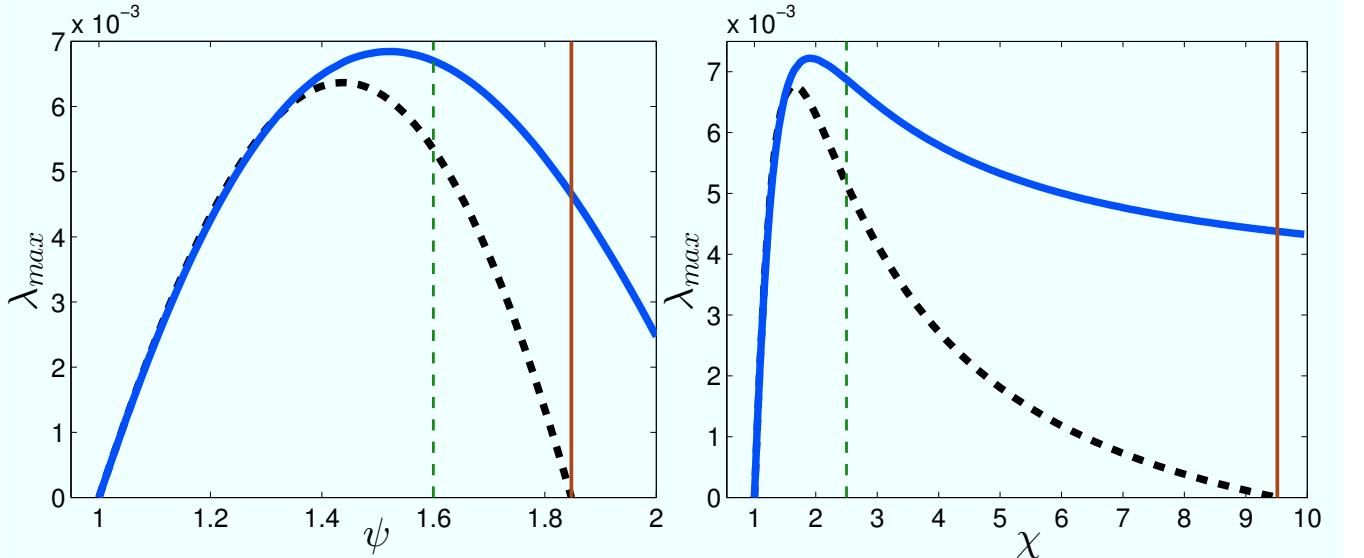

FIG. 3. The maximal growth rate λ_{max} as a function of ψ for $\chi=1$ (left, solid line) and as a function of χ for $\psi=1$ (right, solid line) obtained from numerical solutions of Eq. (7). The dashed lines correspond to the analytic approximation in Eq. (9). The vertical dashed lines mark the contrast values considered in Fig. 2. The vertical solid lines mark the maximal contrast for which Generalized Rayleigh waves exist. We used $\nu^{(1)}=\nu^{(2)}=0.25$ and $f=0.3$ to obtain the results shown in this figure.

rial contrast, important physical quantities such as the maximal growth rate of homogeneous sliding instability modes can exhibit a non-monotonic dependence on the bimaterial contrast. This was done for a regularized Coulomb friction constitutive relation. Does this non-monotonicity persist for other, more realistic, interfacial constitutive relations? To address this question we consider in this section sliding along interfaces described by a generic rate-and-state friction constitutive framework. In particular, we consider the following constitutive framework [10, 49, 60]

$$\tau = f(v,\phi)\,\sigma \qquad \text{and} \qquad \dot{\phi} = g\left(\frac{v\phi}{D}\right)\ , \quad (10)$$

with $g(1)=0$ and $g'(1)<0$. This constitutive framework makes reference to the multi-contact nature of macro-

scopic frictional interfaces, where $\phi(x,t)$ is an internal state field that quantifies the average lifetime of contact asperities in mesoscopic portions of the interface and D is a memory length related to the linear size of contact asperities. For homogeneous steady state sliding at a slip velocity V, we have $\phi = D/V$ (corresponding to $g(1)=0$) and $\tau_0 = f(V, D/V)\sigma_0$, where σ_0 is a constant compressive stress. Since sliding reduces the lifetime of microcontacts, we have $g'(1)<0$.

We are interested in the stability of this homogeneous sliding steady state. To that aim, we perturb Eq. (10) in the form

$$\delta\tau = \delta\sigma_{yx} = -f\delta\sigma_{yy} + \sigma_0\delta f \ . \qquad (11)$$

We then substitute the perturbation expressions for $\delta\sigma_{yx}$ and $\delta\sigma_{yy}$ in terms of $\delta\epsilon$ given in Eq. (6). $\delta f/\delta v$ is expressed in terms of $\delta f/\delta\phi$ by taking the variation of $f(v,\phi)$ around steady state [22, 65]. $\delta f/\delta\phi$ is obtained by taking the variation of $\dot{\phi}$ in Eq. (10) around steady state. Finally, using $\delta v = -i\,k\,z\,c_s^{(1)}\,\delta\epsilon$, δf is expressed in terms of $\delta\epsilon$ and once substituted in Eq. (11) we obtain

$$\gamma\left[G_1(z) - ifG_2(z)\right] + iz\frac{\Delta - iqz}{1 - iqz} = 0 \ , \qquad (12)$$

where the dimensionless wavenumber $q = \frac{kDc_s^{(1)}}{|g'(1)|V}$ is *different* from the corresponding quantity in Eq. (7) as different normalization is used.

While Eq. (7) depends on a single interfacial parameter f, Eq. (12) depends on the following three dimensionless interfacial parameters

$$f(v,\phi), \quad \gamma \equiv \frac{\mu}{\sigma_0\,c_s^{(1)}\,\frac{\partial f(v,\phi)}{\partial v}}, \quad \Delta \equiv \frac{df(v,\phi(v))}{dv}\bigg/\frac{\partial f(v,\phi)}{\partial v} ,$$

$$(13)$$

all evaluated at steady state, i.e. at $v=V$ and $\phi = D/V$. $f(v,\phi)$ is simply the friction coefficient at steady state. γ quantifies the ratio between the radiation damping coefficient $\mu/c_s^{(1)}$ [27, 59, 61], the normal stress σ_0 and the instantaneous response of the interface to slip velocity variations $\frac{\partial f}{\partial v}$ [22]. The latter is generically positive, $\frac{\partial f}{\partial v}>0$, which is also known as the "direct effect" [10]. Δ is the ratio between the steady state variation of the friction coefficient, $\frac{df}{dv}$, and $\frac{\partial f}{\partial v}$ [22]. $\frac{df}{dv}$ can be both negative and positive, also for the very same interface at different steady state sliding velocities V [9]. As we would like friction to be stabilizing such that the bimaterial effect is the only destabilizing process in the problem, we choose $\frac{df}{dv}>0$. That is, we perform the analysis for steady state velocity-strengthening friction.

We are now interested in studying the dependence of the solutions of Eq. (12) on the bimaterial contrast, where the latter is quantified here by setting $\chi = 1$ and $\nu^{(1)} = \nu^{(2)} = 0.25$, and varying ψ. Obtaining analytic solutions to Eq. (12), even approximate, is a very serious mathematical challenge and consequently we resort to numerical solutions. In the $\psi \to 1$ limit, i.e. in the absence of a bimaterial contrast, homogeneous sliding is unconditionally stable because friction is intrinsically stabilizing in this problem. That is, all wavenumbers q feature a negative growth rate $\lambda(q)=q\Im[z]<0$ in the $\psi \to 1$ limit. As ψ is increased, the destabilizing bimaterial effect competes with the stabilizing friction, and beyond a certain level of bimaterial contrast unstable solutions emerge. That is, above a certain threshold value of ψ, there exists a range of wavenumbers q for which $\lambda > 0$. Examples of such solutions are shown in Fig. 4 (left). In fact, we have found two families (branches) of unstable solutions to Eq. (12), which emerge at different threshold values of ψ. Each member of these two families of unstable solutions, as demonstrated in Fig. 4 (left), features a maximal growth rate, λ_{max}.

As explained above, for sufficiently small ψ, all perturbation modes are stable. At a threshold value of ψ, unstable solutions emerge, where $\lambda_{max}=0$. As ψ is further increased, λ_{max} becomes finite. Is λ_{max} a monotonically increasing function of ψ? To address this question, we plot in Fig. 4 (right) λ_{max} as a function of ψ, for fixed values of f, γ and Δ (see figure caption). We observe that λ_{max} exhibits a non-monotonic dependence on the bimaterial contrast ψ, similarly to the non-monotonic behavior observed in the regularized Coulomb friction analysis presented in Fig. 3. Therefore, for two very different interfacial constitutive relations — a regularized Coulomb friction and velocity-strengthening rate-and-state friction — important physical quantities exhibit a non-monotonic dependence on the bimaterial contrast. While we cannot rigorously prove that any physical quantity of interest for a general interfacial constitutive relation exhibits a non-monotonic dependence on the bimaterial contrast, we believe that the results presented in sections IV and V provide strong evidence that this might be the case quite generically. Next, we explore the same question in the context of unsteady nonlinear rupture propagation.

VI. NON-MONOTONICITY OF THE BIMATERIAL EFFECT IN DYNAMIC RUPTURE SIMULATIONS WITH SLIP-WEAKENING FRICTION

The analyses presented in the previous sections focussed on the linear stability of steady state homogeneous sliding along bimaterial interfaces. Our goal here is to extend these analyses to nonlinear rupture propagation, which is relevant to a broad range of frictional and earthquake problems. To that aim, we performed simulations of in-plane dynamic rupture between two half-spaces using the 2D spectral element code SEM2DPACK [7]. As above, the upper half-space features elastic moduli $\mu^{(1)}$ and $\nu^{(1)}$, and lower half-space has $\mu^{(2)}$ and $\nu^{(2)}$. The upper half-space is taken to be more compliant, $\mu^{(1)} < \mu^{(2)}$, and we focus on rupture propagating in the slip direction of the more compliant half-space, referred to as the positive direction.
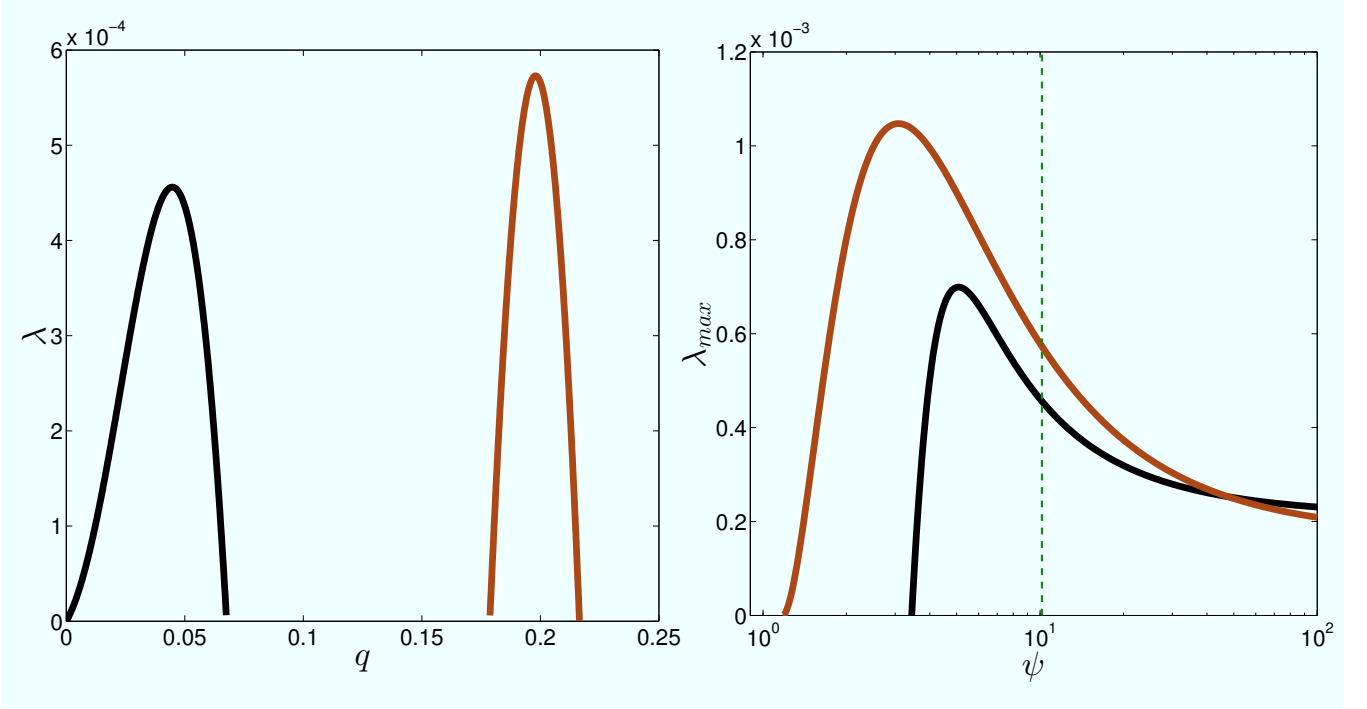
FIG. 4. (left) The instability growth rate λ as a function of the dimensionless wavenumber q obtained from numerical solutions of Eq. (12) with $\psi = 10$, $\chi = 1$, $\gamma = 0.25$, $f = 0.3$, $\Delta = 0.02$, $\nu^{(1)} = 0.28$ and $\nu^{(2)} = 0.37$. Members of two coexisting families of solutions are shown (capturing different ranges of wavenumbers q). (right) The maximal growth rate λ_{max} for the two families of solutions of Eq. (12) as a function of ψ (the rest of the parameters are as in the left panel). The vertical dashed line corresponds to the instability spectra shown in the left panel ($\psi = 10$). Note that the two unstable ($\lambda_{max} > 0$) families of solutions emerge at different threshold $\psi > 1$ values.

The interface between the two half-spaces is characterized by a linear slip-weakening friction law, which is a minimal constitutive framework to account for the transition from stick to slip involved in rupture propagation. In particular, we have

$$\tau \leq f(\epsilon)\,\sigma^* \, , \tag{14}$$

where the inequality holds under stick conditions ($\epsilon = 0$) and the equality holds under slip conditions ($\epsilon > 0$). $f(\epsilon)$ is given by

$$f(\epsilon) = \begin{cases} f_s - (f_s - f_d)\epsilon/D_{\text{sw}} & 0 \leq \epsilon \leq D_{\text{sw}} \\ f_d & \epsilon > D_{\text{sw}} \end{cases} , \tag{15}$$

where f_s and f_d are the static and dynamic friction coefficients, respectively, and D_{sw} is a characteristic slip-weakening distance that controls the transition from f_s to f_d. The regularized normal stress σ^* satisfies

$$\dot{\sigma}^* = -\frac{v + v^*}{L}(\sigma^* - \sigma) \, , \tag{16}$$

which, similarly to Eq. (5), ensures that the problem is well-posed. v^* is chosen to be much smaller than the characteristic slip velocity near the rupture front and the regularization length L satisfies $L \ll D_{\text{sw}}$ such that

σ^* evolves on a timescale shorter than that of the slip-weakening process, making the latter largely independent of the normal stress regularization in Eq. (16). In the slipping region, for $\epsilon > D_{\text{sw}}$, the model bears close similarity to the regularized Coulomb friction model analyzed under steady state sliding conditions in section IV.

The bimaterial contrast is controlled in our simulations by varying the shear wave-speeds ratio $\zeta = c_s^{(2)}/c_s^{(1)} > 1$. This is realized in the following manner: for a given ζ, we first set $\chi = \zeta^{-1}$. Since $\zeta = \sqrt{\psi\chi}$, we have $\psi = \chi^{-3}$. Finally, we set $\nu^{(1)} = \nu^{(2)} = 0.25$, use $\mu^{(2)} = \psi\mu^{(1)}$ and select $\mu^{(1)}$ such that $\bar{\mu}_0/\mu^{(0)} \equiv 2\mu^{(1)}G_1(z \to 0)/\mu^{(0)}$ attains a fixed value of $4/3$ (the value of $(1 - \nu)^{-1}$ for $\nu = 0.25$). Here, $\mu^{(0)}$ is a reference shear modulus in the absence of bimaterial contrast, which is used to normalize quantities of stress dimensions, and $\bar{\mu}_0(\mu^{(1)}, \nu^{(1)}, \mu^{(2)}, \nu^{(2)})$ represents the effective shear modulus for the bimaterial problem [64]. The motivation behind keeping $\bar{\mu}_0$ constant, while varying ζ, χ and ψ as just explained, is that it may help reducing trivial dependencies on the bimaterial contrast and hence revealing potentially less trivial dependencies. In particular, it has been suggested that $\bar{\mu}_0$ affects the rupture nucleation length L_c in the bimaterial problem in much the same way as the ordinary shear modulus μ affects it in the homogeneous materials problem [64]. Consequently, rupture in our simulations

is initiated by over-stressing a nucleation zone of length L_c slightly above the static friction level. The nucleation length L_c is estimated using the Uenishi-Rice length for homogeneous material interfaces [77], where the combination $\mu/(1-\nu)$ of the ordinary shear modulus μ and Poisson's ratio ν is replaced by $\bar{\mu}_0$ [64]. That is, we use $L_c = \frac{1.158\,\bar{\mu}_0 D_{\text{SW}}}{\sigma_0(f_s - f_d)}$, where σ_0 is the magnitude of the applied normal stress, as above. Outside the nucleation zone, an initial shear stress of magnitude τ_0, which lies between the static and dynamic friction levels, is applied.

In our simulations, velocities and stresses are measured relative to the shear wave-speed and the reference shear modulus $\mu^{(0)}$ in the absence of bimaterial contrast ($\zeta = 1$), respectively, and lengths are measured relative to the slip-weakening length D_{SW}. In these units, we set $L = 0.2$ and $v^* = 0.01$, in addition to $f_s = 0.6$ and $f_d = 0.3$. The initial shear stress in the nucleation zone is set to $0.61\sigma_0$ and the shear stress outside the nucleation zone to $\tau_0 = 0.4071\sigma_0$. Finally, the nucleation length is set to $L_c = 5.16$ and $x = 0$ is located at the middle of the nucleation zone. We follow rupture propagation in the positive direction by tracking the spatiotemporal evolution of both the slip velocity $v(x,t)$ and the magnitude of the normal stress reduction $\Delta\sigma(x,t) > 0$, where $t = 0$ is the nucleation time, for various bimaterial contrasts $\zeta \geq 1$.

Our goal now is to define rupture-related quantities that are sensitive to the bimaterial effect in order to study their dependence on the bimaterial contrast. Unlike the analyses presented in previous sections, where the dependence on the bimaterial contrast of various time-independent quantities — such as the instability growth rate — was cleanly defined, rupture propagation is an intrinsically time-dependent process that in many cases does not reach steady state. Hence, the bimaterial contrast may affect different stages of rupture, such as nucleation and post-nucleation propagation style (e.g. sub-shear vs. super-shear, fault opening vs. no fault opening), where early-time dynamics affect later times. To minimize these potentially intervening effects, we (i) use a nucleation length that corresponds to a fixed effective shear modulus $\bar{\mu}_0$ (as explained above) (ii) limit ourselves to the regime where no fault opening takes place and (iii) force the physical quantities of interest to be independent of ζ at some point in time or at a fixed rupture propagation distance by a proper normalization choice.

In particular, we calculate the spatial maximum of the slip velocity $v(x,t)$ at different times, $\max_x[v(x,t)]$, and normalize it by $\max_x[v(x,t=25)]$. Therefore, by construction, this normalized quantity equals unity independently of ζ at $t = 25$. The ζ dependence of this normalized quantity as time progresses, $t > 25$, is plotted in Fig. 5a (left). It is observed that $\max_x[v(x,t)]/\max_x[v(x,t=25)]$ becomes a non-monotonic function of ζ with increasing time. The maximum of this function, which exhibits a rather weak dependence on time once it appears, occurs at a ζ value which is close to the prediction in Fig. 3 (recall that $\zeta = \sqrt{\psi\chi}$ and that $\chi = 1$ was used there). In Fig. 5a (right), we plot the spatial maximum of the normal stress reduction $\Delta\sigma(x,t)$ at different times, $\max_x[\Delta\sigma(x,t)]$, normalized by $\max_x[\Delta\sigma(x,t=25)]$ (except for $\zeta = 1$, where $\Delta\sigma = 0$ due to the absence of a bimaterial contrast), as a function of ζ. It is observed that $\max_x[\Delta\sigma(x,t)]/\max_x[\Delta\sigma(x,t=25)]$ becomes a non-monotonic function of ζ with increasing time, attaining a maximum at a contrast level similar to the one observed in Fig. 5a (left). In Fig. 5b, we plot the temporal maximum of the slip velocity (left) at different fixed locations on the fault (corresponding to a fixed rupture propagation distance in the positive direction), $\max_t[v(x,t)]$, and of the normal stress reduction (right), $\max_t[\Delta\sigma(x,t)]$, both normalized by the corresponding values at $x = 10$, as a function of ζ. Both quantities develop a non-monotonic dependence on ζ with increasing rupture propagation distance. All in all, the results presented in Fig. 5 provide evidence that the non-monotonicity of the bimaterial effect persists in non-steady, transient frictional dynamics.

The growth rate of both slip velocity and changes in normal stress in Fig. 5 are peaked at ζ values between 1.3 and 1.4, rather than at the maximal used value of 1.7. This is similar to the results of *Ben-Zion and Andrews* [14] on the amplification of slip velocity with propagation distance vs. bimaterial contrast in simulations with a constant Coulomb friction. The non-monotonicity observed in Fig. 5 can be at least partially rationalized through an analytic estimation developed in *Rubin and Ampuero* [64] for linear slip-weakening friction. There, cf. Eq. (12), the normal stress reduction is expressed as a function of $\bar{\mu}/\mu^* = 2G_1(z = -v_r/c_s^{(1)})/G_2(z = -v_r/c_s^{(1)}) \equiv \mathcal{G}$ in the approximated form $\Delta\sigma \sim (\mathcal{G} - f)^{-1}$, where v_r is the rupture propagation velocity. For small rupture velocities, $\mathcal{G}$ is positive and larger than f, and is a decreasing function of the bimaterial contrast. This implies that $\Delta\sigma$ is a monotonically increasing function of the contrast for small rupture velocities. For large rupture velocities, relevant for the rupture propagation velocities v_r in the simulations analyzed in Fig. 5, $\mathcal{G}$ can equal f — say at ζ_f — where the expression for $\Delta\sigma$ formally diverges. For $\zeta > \zeta_f$, $\mathcal{G} > f$ and is an increasing function of the bimaterial contrast. This implies that $\Delta\sigma$ for large velocities is a monotonically decreasing function of the contrast for $\zeta > \zeta_f$, consistent with the decreasing functions of ζ observed in Fig. 5 after the peak value. For $\zeta < \zeta_f$, $\mathcal{G}$ is temporarily larger than f due to early-time slow rupture acceleration, but may approach f at later stages of rupture evolution. This is consistent with the delayed growth of $\Delta\sigma$ for small ζ observed in Fig. 5 to the left of the peak value. Taken together, the analytic estimate $\Delta\sigma \sim (\mathcal{G} - f)^{-1}$ may rationalize the non-monotonicity observed in Fig. 5.

VII. SUMMARY AND DISCUSSION

The analyses performed in this paper provide a series of analytic and numerical results on the dependence of various quantities related to the dynamics of bimaterial fric-
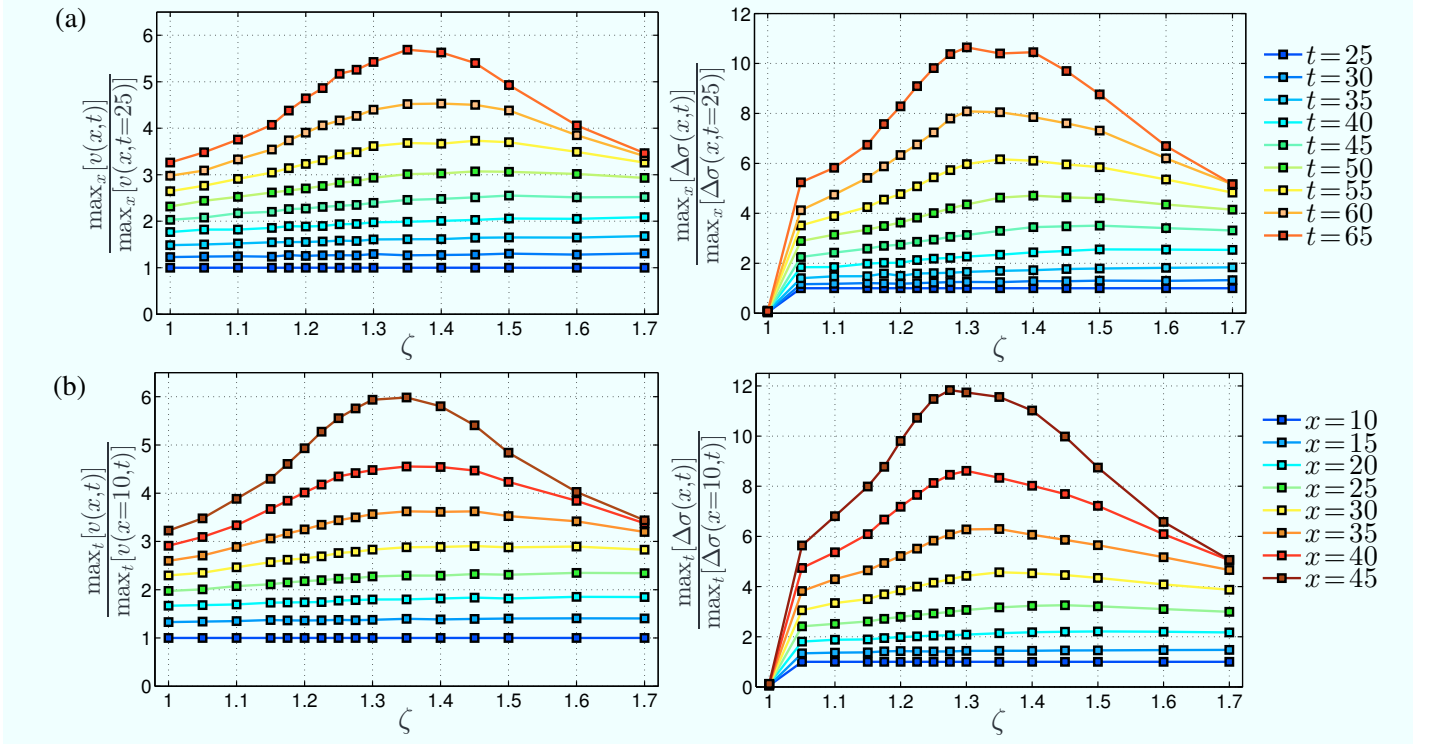
FIG. 5. Results of in-plane rupture simulations using linear slip-weakening friction (see text for details). (a) The spatial maximum of the slip velocity $v(x,t)$ at different times (see legend on the right), $\max_x[v(x,t)]$, normalized by $\max_x[v(x,t=25)]$, as a function of ζ (left). The spatial maximum of the normal stress reduction $\Delta\sigma(x,t)$ at different times (see legend on the right), $\max_x[\Delta\sigma(x,t)]$, normalized by $\max_x[\Delta\sigma(x,t=25)]$ (except for $\zeta=1$, where $\Delta\sigma=0$ due to the absence of a bimaterial contrast), as a function of ζ (right). (b) The temporal maximum of the slip velocity (left) at different fixed locations on the fault (corresponding to a fixed rupture propagation distance in the positive direction, see legend on the right), $\max_t[v(x,t)]$, and of the normal stress reduction (right), $\max_t[\Delta\sigma(x,t)]$, both normalized by the corresponding values at $x=10$, as a function of ζ.

tional interfaces on the degree of contrast across the interface. The results demonstrate that while the bimaterial coupling between interfacial slip and normal stress perturbations is a monotonically increasing function of the bimaterial contrast, when an interfacial constitutive relation (friction law) is considered, various physical quantities exhibit a non-monotonic dependence. This seemingly generic effect emerges both in the context of the stability of steady state sliding and unsteady rupture propagation, using several interfacial constitutive laws including regularized Coulomb friction, rate-and-state friction and slip-weakening friction.

The existence of a non-monotonic dependence of various physical quantities on the bimaterial contrast implies that there exists a level of bimaterial contrast for which the destabilizing bimaterial effect is maximal. The exact contrast level for maximal bimaterial effect may vary from one physical quantity to another and may depend on the interfacial constitutive relation. The existence of a maximum may have significant implications for interfacial dynamics and rupture, since the magnitude of the bimaterial effect strongly affects the degree of dynamic changes in normal stress and elastodynamic fric-

tional weakening. This, in turn, controls the stability of sliding, style of rupture, frequency range and spatial pattern of radiated waves, amount of frictional heat dissipation accompanying interfacial rupture, and other issues discussed in *Ben-Zion and Andrews* [14] and later papers.

The contrast of seismic velocities across the seismogenic sections (e.g. depth >3 km) of large natural faults is typically $10-20\%$ or less [e.g. 5, 18, 44]. The velocity contrasts between the edges of core damage zones of faults and the surrounding rock may be 50% or more, but these damage zones are usually limited to the top few km of the crust [e.g. 19, 87]. In the context of laboratory experiments, where the bimaterial contrast is externally controlled by the selection of the pair of materials to be used, our results can guide the selection of a bimaterial contrast so as to maximize the sensitivity to the bimaterial effect. Laboratory experiments can also systematically test our predictions by controllably varying the bimaterial contrast. It is important to note in this context that the destabilizing bimaterial effect and related dynamic phenomena evolve with propagation distance and time [e.g. 3, 8, 13, 58]. Focusing on the rup-

ture propagation problem, prominent bimaterial effects as observed in Fig. 5 require either large rupture velocity or long propagation distance [15], which in general depend on additional factors such as rupture nucleation, background stress and strain rate, and fault constitutive laws [e.g. 6, 69, 73]. In the context of glacial earthquakes with a large property contrast between ice and rock, our results may partly explain why the degree of slip instability is often limited compared to typical tectonic earthquakes [81], though other factors (e.g. loading style, ice melting, drainage) can also play an important role.

Some of the analyses performed in this study can be extended to other configurations producing dynamic changes in normal stress along a frictional interface. Examples include contrast in poroelastic properties across faults [32] and asymmetric geometrical properties of the solids across faults [4], where the latter are directly relevant to geometric variations and free surface effects on dipping faults [35, 51]. In this context, it is interesting to note that several of these effects, and the elastodynamic bimaterial effect analyzed in this study, can coexist at the shallow portions of subduction zones. Moreover, the degree of geometric and/or bimaterial contrast across the subduction plate interface can vary as a function of distance towards the trench. These factors may complicate

the interplay between dynamic change of normal stress and friction along the plate interface, and the displacement partitioning between the overriding plate and the subducting plate.

Finally, we emphasize that our results on the non-monotonic dependence of various quantities on the bimaterial contrast are based on separate analyses of the stability of steady sliding against linear perturbations and of non-steady nonlinear rupture propagation, focusing primarily on the sub-shear regime. Future theoretical and experimental studies can improve the understanding of the dynamics leading to non-monotonicity and other aspects of bimaterial ruptures by considering additional ingredients known to affect rupture behavior, such as nucleation process and properties of the initial stress field, and examining results also for the super-shear rupture regime and negative propagation direction.

APPENDIX: THE ELASTODYNAMIC TRANSFER FUNCTIONS G_1 AND G_2

The elastodynamic transfer functions G_1 and G_2, introduced in section II and used throughout the paper, take the following form

$$G_1 = \frac{\chi\psi^2 z^2 R^{(1)} R^{(2)} \left(\chi\psi^2 R^{(2)}\alpha_d^{(1)} + R^{(1)}\alpha_d^{(2)}\right)}{z^4 \left(\chi\psi^2 R^{(2)}\alpha_d^{(1)} + R^{(1)}\alpha_d^{(2)}\right)\left(\chi\psi^2 R^{(2)}\alpha_s^{(1)} + R^{(1)}\alpha_s^{(2)}\right) - \chi^2\psi^2 \left(P^{(2)} R^{(1)} - \psi P^{(1)} R^{(2)}\right)^2} \, ,$$

$$G_2 = \frac{\chi^2\psi^3 R^{(1)} R^{(2)} \left(P^{(2)} R^{(1)} - \psi P^{(1)} R^{(2)}\right)}{z^4 \left(\chi\psi^2 R^{(2)}\alpha_d^{(1)} + R^{(1)}\alpha_d^{(2)}\right)\left(\chi\psi^2 R^{(2)}\alpha_s^{(1)} + R^{(1)}\alpha_s^{(2)}\right) - \chi^2\psi^2 \left(P^{(2)} R^{(1)} - \psi P^{(1)} R^{(2)}\right)^2} \, ,$$

where $P^{(\mathrm{n})} \equiv 2\alpha_d^{(\mathrm{n})}\alpha_s^{(\mathrm{n})} - \left(\alpha_s^{(\mathrm{n})2} + 1\right)$ and $R^{(\mathrm{n})} \equiv 4\alpha_d^{(\mathrm{n})}\alpha_s^{(\mathrm{n})} - \left(\alpha_s^{(\mathrm{n})2} + 1\right)^2$, with $n = 1, 2$.

ACKNOWLEDGMENTS

[1] Achenbach, J. D. (1975), Plane harmonic waves in elastic half-spaces, in *Wave Propagation in Elastic Solids*, chap. 5, pp. 165–201, Elsevier, doi:10.1016/B978-0-7204-0325-1.50010-2.

[2] Achenbach, J. D., and H. I. Epstein (1967), Dynamic Interaction of a Layer and a Half-Space, *Journal of the Engineering Mechanics Division*, *93*(5), 27–42.

[3] Adams, G. G. (1995), Self-Excited Oscillations of Two Elastic Half-Spaces Sliding With a Constant Coefficient of Friction, *Journal of Applied Mechanics*, *62*(4), 867, doi:10.1115/1.2896013.

[4] Aldam, M., Y. Bar-Sinai, I. Svetlizky, E. A. Brener, J. Fineberg, and E. Bouchbinder (2016), Frictional Sliding without Geometrical Reflection Symmetry, *Physical Review X*, *6*(4), 041023, doi:10.1103/PhysRevX.6.041023.

[5] Allam, A. A., Y. Ben-Zion, and Z. Peng (2014), Seismic Imaging of a Bimaterial Interface Along the Hayward Fault, CA, with Fault Zone Head Waves and Direct P Arrivals, *Pure and Applied Geophysics*, *171*(11), 2993–

3011, doi:10.1007/s00024-014-0784-0.

[6] Ampuero, J.-P., and Y. Ben-Zion (2008), Cracks, pulses and macroscopic asymmetry of dynamic rupture on a bimaterial interface with velocity-weakening friction, *Geophysical Journal International*, *173*(2), 674–692, doi: 10.1111/j.1365-246X.2008.03736.x.

[7] Ampuero, J.-P. (2002), Etude physique et numérique de la nucléation des séismes, Ph.D. thesis, Université Paris 7, Denis Diderot, Paris, France.

[8] Andrews, D. J., and Y. Ben-Zion (1997), Wrinkle-like slip pulse on a fault between different materials, *Journal of Geophysical Research: Solid Earth*, *102*(B1), 553–571, doi:10.1029/96JB02856.

[9] Bar-Sinai, Y., R. Spatschek, E. A. Brener, and E. Bouchbinder (2014), On the velocity-strengthening behavior of dry friction, *Journal of Geophysical Research: Solid Earth*, *119*(3), 1738–1748, doi:10.1002/2013JB010586.

[10] Baumberger, T., and C. Caroli (2006), Solid friction from stickslip down to pinning and aging, *Advances in Physics*, *55*(3-4), 279–348, doi:10.1080/00018730600732186.

[11] Ben-Zion, Y. (1989), The response of two joined quarter spaces to SH line sources located at the material discontinuity interface, *Geophysical Journal International*, *98*(2), 213–222, doi:10.1111/j.1365-246X.1989.tb03346.x.

[12] Ben-Zion, Y. (1990), The response of two half spaces to point dislocations at the material interface, *Geophysical Journal International*, *101*(3), 507–528, doi: 10.1111/j.1365-246X.1990.tb05567.x.

[13] Ben-Zion, Y. (2001), Dynamic ruptures in recent models of earthquake faults, *Journal of the Mechanics and Physics of Solids*, *49*(9), 2209–2244, doi:10.1016/S0022-5096(01)00036-9.

[14] Ben-Zion, Y., and D. J. Andrews (1998), Properties and implications of dynamic rupture along a material interface, *Bulletin of the Seismological Society of America*, *88*(4), 1085—-1094.

[15] Ben-Zion, Y., and Y. Huang (2002), Dynamic rupture on an interface between a compliant fault zone layer and a stiffer surrounding solid, *Journal of Geophysical Research*, *107*(B2), 2042, doi:10.1029/2001JB000254.

[16] Ben-Zion, Y., and P. Malin (1991), San Andreas Fault Zone Head Waves Near Parkfield, California, *Science*, *251*(5001), 1592–1594, doi: 10.1126/science.251.5001.1592.

[17] Ben-Zion, Y., and Z. Shi (2005), Dynamic rupture on a material interface with spontaneous generation of plastic strain in the bulk, *Earth and Planetary Science Letters*, *236*(1-2), 486–496, doi:10.1016/j.epsl.2005.03.025.

[18] Ben-Zion, Y., S. Katz, and P. Leary (1992), Joint inversion of fault zone head waves and direct P arrivals for crustal structure near major faults, *Journal of Geophysical Research: Solid Earth*, *97*(B2), 1943–1951, doi: 10.1029/91JB02748.

[19] Ben-Zion, Y., Z. Peng, D. Okaya, L. Seeber, J. G. Armbruster, N. Ozer, A. J. Michael, S. Baris, and M. Aktar (2003), A shallow fault-zone structure illuminated by trapped waves in the Karadere-Duzce branch of the North Anatolian Fault, western Turkey, *Geophysical Journal International*, *152*(3), 699–717, doi: 10.1046/j.1365-246X.2003.01870.x.

[20] Bhat, H. S., R. Biegel, A. Rosakis, and C. Sammis (2010), The effect of asymmetric damage on dynamic shear rupture propagation II: With mismatch in bulk elasticity, *Tectonophysics*, *493*(3-4), 263–271, doi:

[21] Bohnhoff, M., P. Martínez-Garzón, F. Bulut, E. Stierle, and Y. Ben-Zion (2016), Maximum earthquake magnitudes along different sections of the North Anatolian fault zone, *Tectonophysics*, *674*, 147–165, doi: 10.1016/j.tecto.2016.02.028.

[22] Brener, E. A., M. Weikamp, R. Spatschek, Y. Bar-Sinai, and E. Bouchbinder (2016), Dynamic instabilities of frictional sliding at a bimaterial interface, *Journal of the Mechanics and Physics of Solids*, *89*, 149–173, doi: 10.1016/j.jmps.2016.01.009.

[23] Dade, B. W., and H. E. Huppert (1998), Long-runout rockfalls, *Geology*, *26*(9), 803, doi:10.1130/0091-7613(1998)026¡0803:LRR¿2.3.CO;2.

[24] Brietzke, G. B., and Y. Ben-Zion (2006), Examining tendencies of in-plane rupture to migrate to material interfaces, *Geophysical Journal International*, *167*(2), 807–819, doi:10.1111/j.1365-246X.2006.03137.x.

[25] Calderoni, G., A. Rovelli, Y. Ben-Zion, and R. Di Giovambattista (2015), Along-strike rupture directivity of earthquakes of the 2009 L'Aquila, central Italy, seismic sequence, *Geophysical Journal International*, *203*(1), 399–415, doi:10.1093/gji/ggv275.

[26] Cochard, A., and J. R. Rice (2000), Fault rupture between dissimilar materials: Ill-posedness, regularization, and slip-pulse response, *Journal of Geophysical Research: Solid Earth*, *105*(B11), 25,891–25,907, doi: 10.1029/2000JB900230.

[27] Crupi, P., and A. Bizzarri (2013), The role of radiation damping in the modeling of repeated earthquake events, *Annals of Geophysics*, *56*(1), R0111, doi:10.4401/ag-6200.

[28] DeDontney, N., E. L. Templeton-Barrett, J. R. Rice, and R. Dmowska (2011), Influence of plastic deformation on bimaterial fault rupture directivity, *Journal of Geophysical Research*, *116*(B10), B10,312, doi: 10.1029/2011JB008417.

[29] Dor, O., T. K. Rockwell, and Y. Ben-Zion (2006), Geological Observations of Damage Asymmetry in the Structure of the San Jacinto, San Andreas and Punchbowl Faults in Southern California: A Possible Indicator for Preferred Rupture Propagation Direction, *Pure and Applied Geophysics*, *163*(2-3), 301–349, doi:10.1007/s00024-005-0023-9.

[30] Dor, O., C. Yildirim, T. K. Rockwell, Y. Ben-Zion, O. Emre, M. Sisk, and T. Y. Duman (2008), Geological and geomorphologic asymmetry across the rupture zones of the 1943 and 1944 earthquakes on the North Anatolian Fault: possible signals for preferred earthquake propagation direction, *Geophysical Journal International*, *173*(2), 483–504, doi:10.1111/j.1365-246X.2008.03709.x.

[31] Dowson, D. (1979), *History of tribology*, Addison-Wesley Longman Limited.

[32] Dunham, E. M., and J. R. Rice (2008), Earthquake slip between dissimilar poroelastic materials, *Journal of Geophysical Research*, *113*(B9), B09,304, doi: 10.1029/2007JB005405.

[33] Eberhart-Phillips, D., and A. J. Michael (1993), Three-dimensional velocity structure, seismicity, and fault structure in the Parkfield Region, central California, *Journal of Geophysical Research*, *98*(B9), 15,737, doi: 10.1029/93JB01029.

[34] Erickson, B. A., and S. M. Day (2016), Bimaterial effects in an earthquake cycle model using rate-and-state

friction, *Journal of Geophysical Research: Solid Earth*, *121*(4), 2480–2506, doi:10.1002/2015JB012470.

[35] Gabuchian, V., A. J. Rosakis, H. S. Bhat, R. Madariaga, and H. Kanamori (2017), Experimental evidence that thrust earthquake ruptures might open faults, *Nature*, *545*(7654), 336–339, doi:10.1038/nature22045.

[36] Geubelle, P., and J. R. Rice (1995), A spectral method for three-dimensional elastodynamic fracture problems, *Journal of the Mechanics and Physics of Solids*, *43*(11), 1791–1824, doi:10.1016/0022-5096(95)00043-I.

[37] Harris, R. A., and S. M. Day (1997), Effects of a low-velocity zone on a dynamic rupture, *Bulletin of the Seismological Society of America*, *87*(5), 1267–1280.

[38] Huang, Y., J.-P. Ampuero, and D. V. Helmberger (2014), Earthquake ruptures modulated by waves in damaged fault zones, *Journal of Geophysical Research: Solid Earth*, *119*(4), 3133–3154, doi:10.1002/2013JB010724.

[39] Landau, L., and E. Lifshitz (1986), *Theory of Elasticity, Third Edition: Volume 7 (Course of Theoretical Physics)*, Butterworth-Heinemann.

[40] Lay, T. (2015), The surge of great earthquakes from 2004 to 2014, *Earth and Planetary Science Letters*, *409*, 133–146, doi:10.1016/j.epsl.2014.10.047.

[41] Legros, F. (2002), The mobility of long-runout landslides, *Engineering Geology*, *63*(3-4), 301–331, doi:10.1016/S0013-7952(01)00090-4.

[42] Lengliné, O., and J.-L. Got (2011), Rupture directivity of microearthquake sequences near Parkfield, California, *Geophysical Research Letters*, *38*(8), n/a–n/a, doi:10.1029/2011GL047303.

[43] Lewis, M. A., Z. Peng, Y. Ben-Zion, and F. L. Vernon (2005), Shallow seismic trapping structure in the San Jacinto fault zone near Anza, California, *Geophysical Journal International*, *162*(3), 867–881, doi:10.1111/j.1365-246X.2005.02684.x.

[44] Lewis, M. A., Y. Ben-Zion, and J. J. McGuire (2007), Imaging the deep structure of the San Andreas Fault south of Hollister with joint analysis of fault zone head and direct P arrivals, *Geophysical Journal International*, *169*(3), 1028–1042, doi:10.1111/j.1365-246X.2006.03319.x.

[45] Lipovsky, B. P., and E. M. Dunham (2016), Tremor during ice-stream stick slip, *The Cryosphere*, *10*(1), 385–399, doi:10.5194/tc-10-385-2016.

[46] Lotto, G. C., E. M. Dunham, T. N. Jeppson, and H. J. Tobin (2017), The effect of compliant prisms on subduction zone earthquakes and tsunamis, *Earth and Planetary Science Letters*, *458*, 213–222, doi:10.1016/j.epsl.2016.10.050.

[47] Lyakhovsky, V., Y. Hamiel, and Y. Ben-Zion (2011), A non-local visco-elastic damage model and dynamic fracturing, *Journal of the Mechanics and Physics of Solids*, *59*(9), 1752–1776, doi:10.1016/j.jmps.2011.05.016.

[48] Lykotrafitis, G., and A. Rosakis (2006), Dynamic sliding of frictionally held bimaterial interfaces subjected to impact shear loading, *Proceedings of the Royal Society A: Mathematical, Physical and Engineering Sciences*, *462*(2074), 2997–3026, doi:10.1098/rspa.2006.1703.

[49] Marone, C. (1998), The effect of loading rate on static friction and the rate of fault healing during the earthquake cycle, *Nature*, *391*(6662), 69–72, doi:10.1038/34157.

[50] Mitchell, T., Y. Ben-Zion, and T. Shimamoto (2011), Pulverized fault rocks and damage asymmetry along the Arima-Takatsuki Tectonic Line, Japan, *Earth and Planetary Science Letters*, *308*(3-4), 284–297, doi:10.1016/j.epsl.2011.04.023.

[51] Oglesby, D. D. (1998), Earthquakes on Dipping Faults: The Effects of Broken Symmetry, *Science*, *280*(5366), 1055–1059, doi:10.1126/science.280.5366.1055.

[52] Ozakin, Y., Y. Ben-Zion, M. Aktar, H. Karabulut, and Z. Peng (2012), Velocity contrast across the 1944 rupture zone of the North Anatolian fault east of Ismetpasa from analysis of teleseismic arrivals, *Geophysical Research Letters*, *39*(8), doi:10.1029/2012GL051426.

[53] Paul Winberry, J., S. Anandakrishnan, D. A. Wiens, and R. B. Alley (2013), Nucleation and seismic tremor associated with the glacial earthquakes of Whillans Ice Stream, Antarctica, *Geophysical Research Letters*, *40*(2), 312–315, doi:10.1002/grl.50130.

[54] Persson, B. N. J. (1998), *Sliding friction: physical principles and applications*, Springer Sciense & Buisness Media.

[55] Prakash, V. (1998), Frictional Response of Sliding Interfaces Subjected to Time Varying Normal Pressures, *Journal of Tribology*, *120*(1), 97, doi:10.1115/1.2834197.

[56] Prakash, V., and R. J. Clifton (1992), Pressure-shear plate impact measurement of dynamic friction for high speed machining applications, *Proceedings of the 7th International Congress on Experimental Mechanics*, pp. 8–11.

[57] Prakash, V., and R. J. Clifton (1993), Time resolved dynamic friction measurements in pressure-shear, *Experimental Techniques in the Dynamics of Deformable Solids*, *165*, 33–48.

[58] Ranjith, K., and J. R. Rice (2001), Slip dynamics at an interface between dissimilar materials, *Journal of the Mechanics and Physics of Solids*, *49*(2), 341–361, doi:10.1016/S0022-5096(00)00029-6.

[59] Rice, J. R. (1993), Spatio-temporal complexity of slip on a fault, *Journal of Geophysical Research*, *98*(B6), 9885, doi:10.1029/93JB00191.

[60] Rice, J. R., and A. L. Ruina (1983), Stability of Steady Frictional Slipping, *Journal of Applied Mechanics*, *50*(2), 343, doi:10.1115/1.3167042.

[61] Rice, J. R., N. Lapusta, and K. Ranjith (2001), Rate and state dependent friction and the stability of sliding between elastically deformable solids, *Journal of the Mechanics and Physics of Solids*, *49*(9), 1865–1898, doi:10.1016/S0022-5096(01)00042-4.

[62] Rockwell, T. K., T. E. Dawson, J. Young Ben-Horin, and G. Seitz (2015), A 21-Event, 4,000-Year History of Surface Ruptures in the Anza Seismic Gap, San Jacinto Fault, and Implications for Long-term Earthquake Production on a Major Plate Boundary Fault, *Pure and Applied Geophysics*, *172*(5), 1143–1165, doi:10.1007/s00024-014-0955-z.

[63] Ross, Z. E., and Y. Ben-Zion (2016), Toward reliable automated estimates of earthquake source properties from body wave spectra, *Journal of Geophysical Research: Solid Earth*, *121*(6), 4390–4407, doi:10.1002/2016JB013003.

[64] Rubin, A. M., and J.-P. Ampuero (2007), Aftershock asymmetry on a bimaterial interface, *Journal of Geophysical Research*, *112*(B5), B05,307, doi:10.1029/2006JB004337.

[65] Ruina, A. L. (1983), Slip instability and state variable friction laws, *Journal of Geophysical Research*, *88*(B12), 10,359, doi:10.1029/JB088iB12p10359.

[66] Sandvol, E., K. Al-Damegh, A. Calvert, D. Seber, M. Barazangi, R. Mohamad, R. Gök, N. Türkelli, and C. Gürbüz (2001), Tomographic Imaging of Lg and Sn Propagation in the Middle East, *Pure and Applied Geophysics*, *158*(7), 1121–1163, doi:10.1007/PL00001218.

[67] Satake, K., and Y. Tanioka (1999), Sources of Tsunami and Tsunamigenic Earthquakes in Subduction Zones, *Pure and Applied Geophysics*, *154*(3-4), 467–483, doi: 10.1007/s000240050240.

[68] Şengör, A., O. Tüysüz, C. İmren, M. Sakınç, H. Eyidoğan, N. Görür, X. Le Pichon, and C. Rangin (2005), The North Anatolian fault: A new look, *Annual Review of Earth and Planetary Sciences*, *33*(1), 37–112, doi:10.1146/annurev.earth.32.101802.120415.

[69] Scala, A., G. Festa, and J.-P. Vilotte (2017), Rupture dynamics along bimaterial interfaces: a parametric study of the shear-normal traction coupling, *Geophysical Journal International*, p. ggw489, doi:10.1093/gji/ggw489.

[70] Scholz, C. H. (2002), *The mechanics of earthquakes and faulting*, Cambridge university press.

[71] Scholz, C. H. (2014), The Rupture Mode of the Shallow Large-Slip Surge of the Tohoku-Oki Earthquake, *Bulletin of the Seismological Society of America*, *104*(5), 2627–2631, doi:10.1785/0120140130.

[72] Share, P.-E., Y. Ben-Zion, Z. E. Ross, H. Qiu, and F. Vernon (2017), Internal structure of the San Jacinto fault zone at Blackburn Saddle from seismic data of a linear array, *Geophysical Journal International*, doi: 10.1093/gji/ggx191.

[73] Shi, Z., and Y. Ben-Zion (2006), Dynamic rupture on a bimaterial interface governed by slip-weakening friction, *Geophysical Journal International*, *165*(2), 469–484, doi: 10.1111/j.1365-246X.2006.02853.x.

[74] Shlomai, H., and J. Fineberg (2016), The structure of slip-pulses and supershear ruptures driving slip in bimaterial friction, *Nature Communications*, *7*, 11,787, doi: 10.1038/ncomms11787.

[75] Thomas, M. Y., H. S. Bhat, and Y. Klinger (2017), Effect of Brittle off-fault Damage on Earthquake Rupture Dynamics, in *Fault Zone Dynamic Processes: Evolution of Fault Properties During Seismic Rupture*, chap. 14.

[76] Turcotte, D. L., and G. Schubert (2014), *Geodynamics*, Cambridge University Press.

[77] Uenishi, K., and J. R. Rice (2003), Universal nucleation length for slip-weakening rupture instability under nonuniform fault loading, *Journal of Geophysical Research*, *108*, doi:10.1029/2001JB001681.

[78] Wang, E., and A. M. Rubin (2011), Rupture directivity of microearthquakes on the San Andreas Fault from spectral ratio inversion, *Geophysical Journal International*, *186*(2), 852–866, doi:10.1111/j.1365-246X.2011.05087.x.

[79] Weertman, J. (1963), Dislocations moving uniformly on the interface between isotropic media of different elastic properties, *Journal of the Mechanics and Physics of Solids*, *11*(3), 197–204, doi:10.1016/0022-5096(63)90052-8.

[80] Weertman, J. (1980), Unstable slippage across a fault that separates elastic media of different elastic constants, *Journal of Geophysical Research*, *85*(B3), 1455, doi:10.1029/JB085iB03p01455.

[81] Wiens, D. A., S. Anandakrishnan, J. P. Winberry, and M. A. King (2008), Simultaneous teleseismic and geodetic observations of the stickslip motion of an Antarctic ice stream, *Nature*, *453*(7196), 770–774, doi: 10.1038/nature06990.

[82] Xia, K., A. J. Rosakis, H. Kanamori, and J. R. Rice (2005), Laboratory Earthquakes Along Inhomogeneous Faults: Directionality and Supershear, *Science*, *308*(5722), 681–684, doi:10.1126/science.1108193.

[83] Xu, S., and Y. Ben-Zion (2017), Theoretical constraints on dynamic pulverization of fault zone rocks, *Geophysical Journal International*, p. ggx033, doi: 10.1093/gji/ggx033.

[84] Xu, S., Y. Ben-Zion, and J.-P. Ampuero (2012), Properties of inelastic yielding zones generated by in-plane dynamic rupturesII. Detailed parameter-space study, *Geophysical Journal International*, *191*(3), 1343–1360, doi: 10.1111/j.1365-246X.2012.05685.x.

[85] Xu, S., Y. Ben-Zion, J.-P. Ampuero, and V. Lyakhovsky (2015), Dynamic Ruptures on a Frictional Interface with Off-Fault Brittle Damage: Feedback Mechanisms and Effects on Slip and Near-Fault Motion, *Pure and Applied Geophysics*, *172*(5), 1243–1267, doi:10.1007/s00024-014-0923-7.

[86] Yamashita, T. (2000), Generation of microcracks by dynamic shear rupture and its effects on rupture growth and elastic wave radiation, *Geophysical Journal International*, *143*(2), 395–406, doi:10.1046/j.1365-246X.2000.01238.x.

[87] Yang, H., L. Zhu, and E. S. Cochran (2011), Seismic structures of the Calico fault zone inferred from local earthquake travel time modelling, *Geophysical Journal International*, *186*(2), 760–770, doi:10.1111/j.1365-246X.2011.05055.x.